

Impacts of isolated nucleon-nucleon correlations in relativistic $^{16}\text{O} + ^{16}\text{O}$ collisions

Qi Liu,¹ Hadi Mehrabpour,^{1, 2, *} and Bing-Nan Lu^{3, †}

¹*School of Physics, Peking University, Beijing 100871, China*

²*Center for High Energy Physics, Peking University, Beijing 100871, China*

³*Graduate School of China Academy of Engineering Physics, Beijing 100193, China*

Nucleon-nucleon interactions are fundamental to the nuclear forces operating within the nucleus and play a crucial role in shaping the initial conditions of relativistic ion collisions through two-nucleon correlations. In this paper, we introduce an innovative approach to explore these encoded nucleon-nucleon correlations within advanced *ab-initio* models in the context of relativistic ^{16}O collisions. Our methodology successfully reproduces the structural properties of the nucleonic configurations generated by these models, as well as the distance correlations between the nucleon pairs, denoted as $C(\Delta r)$. By generating nucleon positions that align with authentic configurations and adhering to the constraints imposed by the probability distribution of relative two-nucleon distances, our goal is to better understand nucleon-nucleon interactions within *ab-initio* frameworks.

I. INTRODUCTION

Nucleons within the nucleus do not function as truly independent particles; rather, their strong interactions give rise to correlations in both their positions and momenta, which deviate from the mean-field approximation [1, 2]. As a result, nucleon-nucleon (NN) correlations become a vital component of nuclear physics, capturing the inter-dependent behavior of protons and neutrons within the atomic nucleus [2]. These correlations extend beyond the simplistic independent-particle model, emphasizing the intricate interplay of forces that govern nucleon dynamics [3]. Such interactions are essential to contemporary *ab-initio* models, which seek to elucidate the characteristics of light nuclei, particularly in the context of statistical hadronization and coalescence models [4]. This framework introduces constraints derived from two-body correlation distributions, thereby deepening our understanding of the mechanisms that underpin state-of-the-art models [5, 6].

The study of *ab-initio* models in the context of relativistic nuclear collisions [7] at facilities such as the Brookhaven National Laboratory (RHIC) [8] and the Large Hadron Collider (LHC) [9, 10] represents one of the most compelling avenues in nuclear physics research. Recently, researchers have sought to investigate the structural properties of colliding light nuclei through this approach [11–13]. Their findings highlight the significant impact of NN correlations on the initial state, which in turn influences detector observables. While it is well established in low-energy nuclear physics that structural properties reflect long-range correlations within the nucleus [14], recent studies have underscored the importance of short-range nucleon-nucleon correlations in light nuclei [15]. Short-range correlations can be effectively understood in terms of α -clusters within the light nuclei [16]. The effects of α -clustering have been analyzed

analytically in relation to initial correlators for relativistic collisions involving ^{16}O and ^{20}Ne , as detailed in Ref. [17]. Additionally, Ref. [18] explores the angular structure of many-body correlations using α -clusters for ^8Be . In another study, Ref. [19] isolates the influence of multi-nucleon correlations in relativistic $^{16}\text{O} + ^{16}\text{O}$ collisions by maintaining a fixed one-body density distribution of oxygen, utilizing Skyrme-DFT density profiles with varying tetrahedral deformations. They introduced a compactness parameter to effectively isolate α clusters (multi-nucleon correlations) while keeping the one-body density constant.

In this paper, we present a novel method for analyzing both short- and long-range NN correlations in relativistic light-ion collisions by isolating these correlations¹. We apply our method to investigate NN correlations within two different frameworks used to analyze the collided ^{16}O nucleus: Nuclear Lattice Effective Field Theory (NLEFT) [20, 21] and the Variational Monte Carlo (VMC) method [22]. This approach enables us to explore NN correlations across various Hamiltonians and structural configurations. Both NLEFT and VMC are *ab-initio* models designed to elucidate the properties of ^{16}O . NLEFT employs a pion-less effective field theory Hamiltonian and incorporates a pinhole algorithm to determine the spatial positions of each nucleon. In contrast, VMC constructs the nucleus using the Argonne v18 two-nucleon potential alongside the Urbana X three-nucleon potential. Given that these fundamental nucleon interactions can significantly influence NN correlations, we investigate how they affect the initial conditions of relativistic heavy ion collisions using our proposed method.

* hadi.mehrabpour.hm@gmail.com
† bnlv@gscaep.ac.cn

¹ As this method is being introduced for the first time, our initial study focuses solely on the overall NN correlations as they pertain to observable outcomes, allowing us to evaluate its performance. Consequently, we do not delve into the specific effects of short- and long-range correlations on the correlators at this stage. However, this method can be employed to isolate these correlations for further examination of their distinct impacts on observables.

The structure of this paper is organized as follows: In Section II, we outline the foundational principles of our new method and describe the observables used to assess correlation effects. Section III provides a comprehensive discussion of our findings, while Section IV offers our concluding remarks.

II. METHODOLOGY

It is well known that a one-nucleon distribution, which characterizes the nuclear structure, is necessary for reconstructing the process of a heavy-ion collision. To evaluate the single-particle characteristics of the atomic ground state, this distribution is obtained using the one-body density matrix [14]:

$$\rho(\mathbf{r}) = A \int \prod_{i=2}^A d\mathbf{r}_i |\Psi(\mathbf{r}, \mathbf{r}_2, \dots, \mathbf{r}_A)|^2, \quad (1)$$

where $\Psi(\mathbf{r}, \mathbf{r}_2, \dots, \mathbf{r}_A)$ is the normalized A -nucleon ground-state wave function. It is obtained by implementing realistic short-range correlations, including N -body interactions, on an independent particle wave function [23, 24]. To generate a one-body density concerning NN interactions, Ref.[14] suggests a method based on the Metropolis search for configurations that satisfy the constraints imposed by two-body correlations,

$$C(\mathbf{r}, \mathbf{r}') = A(A-1) \int \prod_{i=3}^A d\mathbf{r}_i |\Psi(\mathbf{r}, \mathbf{r}', \mathbf{r}_3, \dots, \mathbf{r}_A)|^2. \quad (2)$$

In this way, the effects of short-range correlations on the single-particle density are retained. The approximate form of Eq.2 is defined by [14, 25]:

$$C(\Delta r) = 1 - \frac{g(\Delta r)}{g'(\Delta r)}, \quad \Delta r = |\mathbf{r}|, \quad (3)$$

where \mathbf{r} is the relative distance vector. The function $g(\Delta r)$ represents the density distribution of nucleon pairs within the same nucleus (correlated two-body densities), which illustrates the correlation effects. In contrast, the $g'(\Delta r)$ is obtained by selecting nucleon pairs from different nuclei (uncorrelated two-body densities) [26]. The function $C(\Delta r)$ intuitively indicates the differences in distance between nucleons caused by nuclear forces. If $C(\Delta r) > 0$ at a certain location, it suggests that the probability of nucleon pairs appearing at this distance is relatively lower compared with uncorrelated nucleon pairs, reflecting a repulsive interaction at this distance or an attractive interaction elsewhere (which affects the normalized distribution)². Since Eq.3 plays an important

role in explaining event-by-event fluctuations of measured quantities using the Glauber approach [27, 28], we employ it to study the properties generated by different *ab-initio* models. In this way, there are two approaches:

1. Finding the α -cluster parameters by controlling the radial one-nucleon density and incorporating nucleon-nucleon correlations at short-distances (inside a given cluster) and long-distances (between two clusters) [17].
2. Generating samples of nucleons based on a fixed charge density function $\rho(r)$ and the constraints derived directly from the density function $g(\Delta r)$ of nucleus, which accounts for the separation of nucleon pairs Δr .

In this paper, we use the second approach to study the various structures of ^{16}O ³ using the *acceptance-rejection method* (ARM) [29]. This method is a statistical technique used to generate random samples from a target probability distribution by utilizing samples from a proposal distribution. ARM, also known as rejection sampling, is a powerful Monte Carlo method employed to sample from a complex or unknown distribution (the target distribution) by utilizing a simpler distribution⁴ (the proposal distribution) from which sampling is easier. However, its effectiveness can be limited by the choice of proposal distribution and challenges associated with high-dimensional spaces.

Approach: The basic idea is to generate samples from the proposal distribution and then accept or reject these samples based on a specific criterion related to the target distribution. In this method, we consider a 3-parameter Fermi (3pF) density distribution to explain the radial nucleon distribution $\rho(r)$ of oxygen:

$$\rho(r) \propto \frac{1 + w(r^2/R_0^2)}{1 + e^{(r-R_0)/a_0}}, \quad (4)$$

where R_0 denotes the half-width radius, w measures central density depletion, and a_0 characterizes the surface diffuseness. For ^{16}O , we parameterize the 3pF density distribution using $R_0 = 2.608$ fm, $a_0 = 0.513$ fm, and $w = -0.051$ [30]. This allows us to determine the magnitude of \vec{r} concerning the distance of nucleons from the origin $(0, 0, 0)$. In the next step, we randomly generate angle coordinates ($\cos \theta$ and ϕ) for each nucleons without any constraints. Moreover, we need to find the two-body distribution of correlated nucleons $g(\Delta r)$ concerning NLEFT and VMC configurations. The uncorrelated

gle of the nucleons in one nucleus. It is easy to see that these two methods for constructing uncorrelated pairs are equivalent. We should note that in the second way the one-body distribution function in radius is preserved while the azimuthal angle distribution is disrupted.

³ This approach is applicable to other light nuclei, such as ^8Be , ^{12}C and ^{20}Ne .

⁴ Moreover, it works for any distribution in \mathcal{R}^m with a density.

² Another way to obtain uncorrelated nucleon pairs is to calculate the pair distributions after randomly changing the azimuthal an-

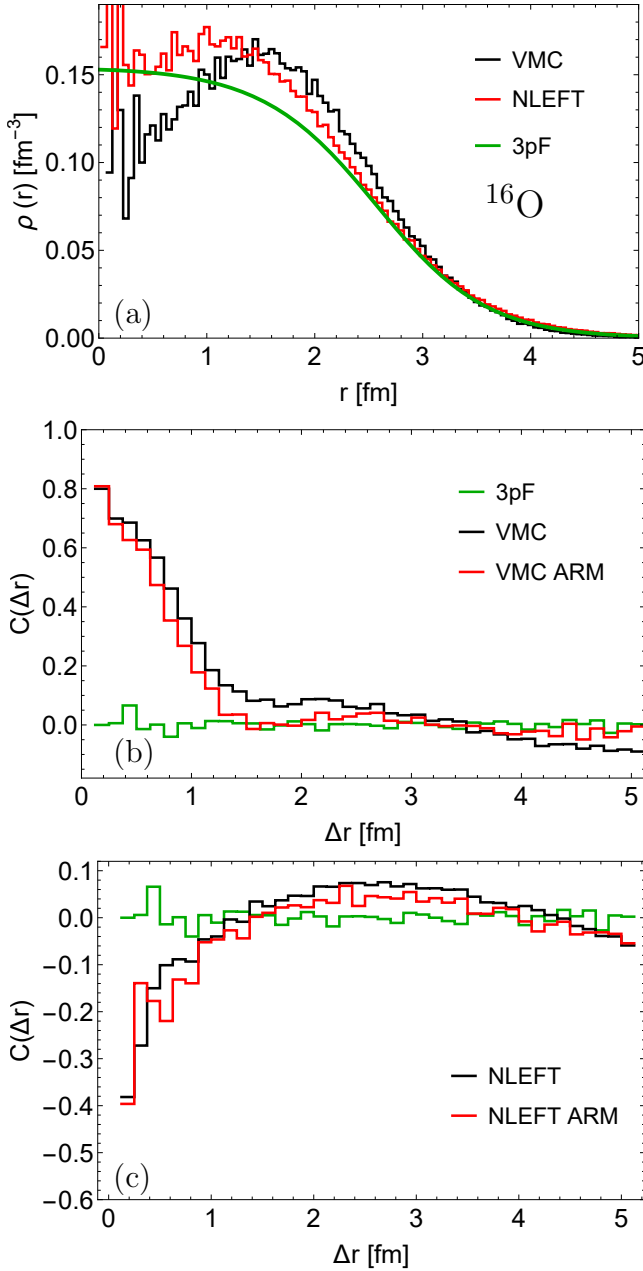


FIG. 1. One-body (panel (a)) and two-body (panels (b) and (c)) distributions of ^{16}O are presented for different configurations. It is important to note that we present the 3pF without re-centering the sampled nucleons. The two-body distributions of ^{16}O are shown for various configurations: original (black lines), uncorrelated (green lines), and ARM (red lines). The results from VMC are depicted in panel (a), while the results from NLEFT are shown in panel (b).

nucleon distribution $g'(\Delta r)$ is selected as the proposal distribution which covers the support of the target distribution $g(\Delta r)$. We must ensure that there exists a constant $M > 0$ such that $g(\Delta r) \leq M \cdot g'(\Delta r)$ for all Δr in the support of g . The expected number of iterations required to accept a draw is M^{-1} . To ensure efficiency,

the optimal choice of M is:

$$M = \sup_{\Delta r} \frac{g(\Delta r)}{g'(\Delta r)},$$

We find that $M = \Delta r_{\text{biggest}}$ can satisfy the inequality of $g(\Delta r) \leq M \cdot g'(\Delta r)$. After generating nucleon configurations starting from the 3pF density, we generate a sample $\Delta r'$ from the proposal distribution $g'(\Delta r)$ as well as a uniform random number U from $\text{Unif}(0, 1)$. The first nucleon, without any changes, will be placed in the configuration. However, we accept other nucleons with relative distances $\Delta r'$ as samples from the target distribution $g(\Delta r')$ if $U \leq (g(\Delta r')/M \cdot g'(\Delta r'))$. If this condition is not met, we reject the sample and repeat the process, regenerating the angular coordinates again. We continue generating samples until we achieve the desired number of samples and repeat the process as necessary.

The radial distribution $\rho(r)$ for VMC (black line), NLEFT (red line), and 3pF (green line) configurations is depicted in Fig.1(a). The differences arise from the distinct structures of these configurations. To analyze these differences, we use the 3pF distribution to collect NN correlations for the NLEFT and VMC configurations. The two-nucleon relative distance distribution $C(\Delta r)$ for VMC is shown in Fig.1(b), while that for NLEFT is presented in Fig.1(c). These modern *ab-initio* models were chosen because VMC is a successful model to explain the RHIC data [8] within the initial state level, and NLEFT models full NN interactions [20, 21]. Moreover, the nucleon-nucleon correlation functions of these two configurations exhibit very different behaviors, particularly in short-range correlations ($\Delta r \leq 1$). The $C(\Delta r)$ function for NLEFT indicates that nucleon pairs are more likely to appear at both short- and long-distances compared to its uncorrelated version. Due to the strong repulsive interactions of nuclear forces at short ranges, VMC shows low pair densities at short distances, while the density at longer ranges increases correspondingly. As can be seen in Figs.1(c), the configurations obtained by ARM can almost capture the NN correlations of NLEFT. Fig.1(b) illustrates that there are differences between VMC and ARM. However, ARM configurations behave similarly to VMC in the short range and to 3pF in the long range. This similarity allows us to study the effects of short- and long-range correlations on observables in relativistic ion collisions, although this aspect is beyond of the scope of the current study.

All the information captured at the density level is necessary for testing in high-energy nuclear collisions as a complementary study. In this way, we use TRENTo [31] to simulate the results of $^{16}\text{O} + ^{16}\text{O}$ collisions at 200 GeV [8] and 5.36 TeV [32] center-of-mass frame. TRENTo is an initial condition model of heavy ion collisions, where the entropy density can be expressed as:

$$\frac{dS}{dy} \propto T_R = \left(\frac{T_A^p + T_B^p}{2} \right)^{\frac{1}{p}},$$

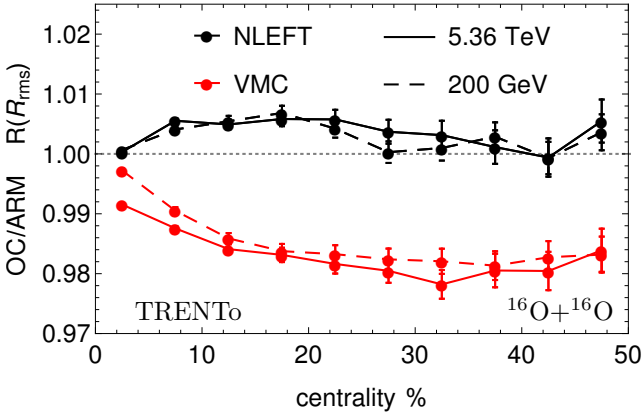


FIG. 2. The transverse size of the systems in the overlap region, R_s , is illustrated. The results from VMC and NLEFT are depicted by red and black lines, respectively. Additionally, the results for O+O collisions at 200 GeV are shown by dashed lines, while those at 5.36 TeV are represented by solid lines.

where T_A and T_B are the thickness functions of two Lorentz-contracted nuclei. The dimensionless parameter p controls physical mechanisms of entropy production; specifically, $p = 1$ exhibits effect similar to those of the Monte Carlo wounded nucleon model, while $p = 0$ results in a single roughly blob-like deposition at the midpoint of the collisions [33, 34]. If p becomes negative, the entropy deposition is suppressed along the direction of the impact parameter. In this study, we generate events with $p = 0$ to exclude the structural properties generated by uncorrelated nucleons or by the 3pF, ARM, and modern *ab-initio* models. We will present the results in the next section.

III. CORRELATORS

In our exploration of how ARM decodes information, we can delve into the event-by-event fluctuations of anisotropic flow V_n and transverse momentum of hadrons p_T . The framework of hydrodynamic response provides a foundation for understanding the total energy density E and initial anisotropies ε_n of the QGP as they relate to p_T and V_n . [35–37]. Therefore, this leads to similar relations for correlators,

$$\langle (\delta[p_T])^2 \rangle \propto \text{var}(E/\langle E \rangle), \quad (5)$$

$$v_n\{2\} \propto \varepsilon_n\{2\}, \quad (6)$$

$$\text{cov}(v_n^2, \delta p_T) \propto \text{cov}(\varepsilon_n^2, \delta E), \quad (7)$$

$$v_n\{4\}/v_n\{2\} \approx \varepsilon_n\{4\}/\varepsilon_n\{2\}, \quad (8)$$

where $\delta\mathcal{O} = (\mathcal{O} - \langle \mathcal{O} \rangle)/\langle \mathcal{O} \rangle$. These correlators assist us to have an estimation from ARM performance. Before diving deeper into these correlators, it is essential to confirm that the information derived from one-body density retains the characteristics of α -cluster configurations

under our specified constraints. To illustrate this, we examine the initial transverse size of the fireball, denoted as R_s , which is calculated using the following equation [38, 39]:

$$R_s^2 = 2 \frac{\int_{x,y} (x^2 + y^2) s(x, y)}{\int_{x,y} s(x, y)}, \quad (9)$$

where $s(x, y)$ present the entropy density within the overlap zone⁵. It is worth noting that in head-on collisions, we can extract the nucleus size from Eq.9, which serves as a reliable predictor of information related to $[p_T]$ [35]. In Fig.2, we present the TRENTo results of R_s , comparing the original configurations (OC) with ARM for NLEFT (black lines) and VMC (red lines) at energies of 200 GeV (dashed lines) and 5.36 TeV (solid lines). The results show that the difference between OC and ARM can be reach up to 2% for VMC and about 1% for NLEFT. The more significant deviation observed in VMC arises from its radial distribution being notably different from that of the 3pF. Nevertheless, our method demonstrates an impressive accuracy of over 98% in capturing the size of the systems created in the overlap zone. Additionally, while there is a slight sensitivity to the collision energies in central collisions for VMC, this remains around 1%.

Two-particle correlators: As previously discussed, the structures of the collided nuclei within the overlap zone can be effectively excluded from flow anisotropy within the hydrodynamic framework. Consequently, the initial special anisotropies ε_n ,

$$\varepsilon_n = \frac{\int_{x,y} (x + iy)^n s(x, y)}{\int_{x,y} (x^2 + y^2)^{n/2} s(x, y)}, \quad \varepsilon_n = |\mathcal{E}_n|, \quad (10)$$

serves as optimal observables for probing the nuclear structures in the initial state [40]. This prompts us to explore the structural properties of nuclei encoded by ARM through these quantities. In Figs.3(a) and 3(d), we present the calculated $\varepsilon_2\{2\} = \langle \varepsilon_2^2 \rangle^{1/2}$ for collision energies of 200 GeV and 5.36 TeV, respectively. The upper plots illustrate the ratios of configurations— OC (solid lines) and ARM (dashed lines)— to the 3pF, which allows us to assess the NN correlations. Notably, we observe a slight loss of structural information for oxygen following the removal of these NN correlations (3pF). The most significant deviation in $\varepsilon_2\{2\}$ from the NLEFT result occurs within the 5-10% centrality range, reaching approximately 6%. This deviation is primarily attributed to substantial effects stemming from short-distance correlations [13], as illustrated in Fig.1. As demonstrated in Fig.3, ARM captures the influence of short-range correlations on $\varepsilon_2\{2\}$ effectively; however, discrepancies between the OC and ARM configurations arise due to ARM's inability to fully encapsulate all model information. These

⁵ The factor of 2 ensures that for a uniform entropy density $s(x, y)$ within a circle of radius [35].

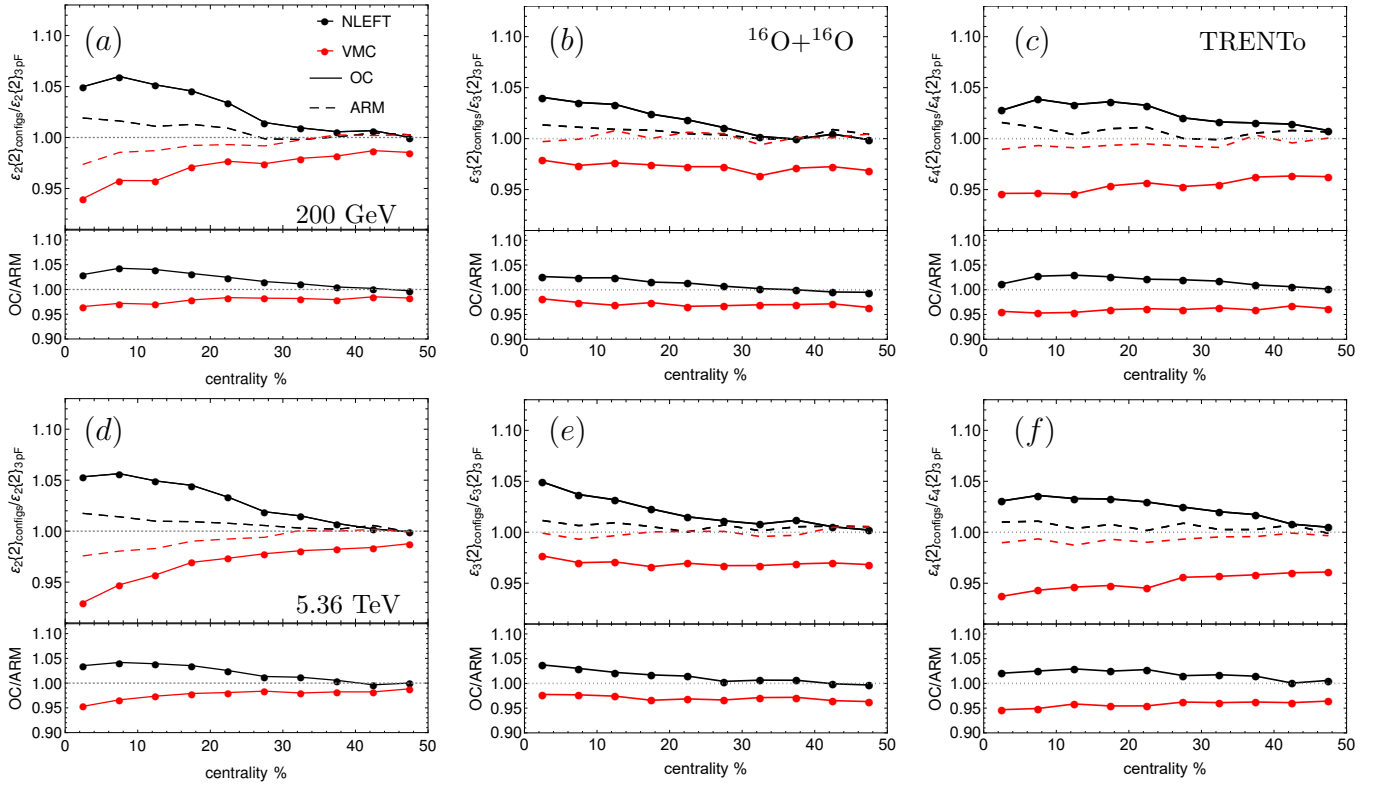


FIG. 3. The effects of nucleon-nucleon (NN) correlations on $\varepsilon_n\{2\}$ obtained from $^{16}\text{O} + ^{16}\text{O}$ collisions are studied for $n = 2$ (left panels), 3 (middle panels), and 4 (right panels). The differences between NLEFT (black lines) and VMC (red lines) with the 3pF model are highlighted. The results from the ARM method are shown as dashed lines. We compare the results of the OC and ARM methods at 200 GeV (top panels) and 5.36 TeV (bottom panels) to examine the sensitivity of our method to collision energies. The bottom panels display the differences between OC and ARM results.

differences are depicted in the lower plots of both panels (a) and (d), where we observe maximum deviations of up to 5% for both NLEFT (black line) and VMC (red line). As we move to mid-central collisions, these deviation exhibit a diminishing trend.

In Fig.3, we present the results for $\varepsilon_3\{2\}$ (middle panels) and $\varepsilon_4\{2\}$ (left panels). Similar to the finding for ε_2 , the ARM calculations effectively capture the general trends observed in the OC results. This can be summarized by examining the ratios $\varepsilon_3\{2\}_{\text{config}}/\varepsilon_3\{2\}_{\text{3pF}}$ and $\varepsilon_4\{2\}_{\text{config}}/\varepsilon_4\{2\}_{\text{3pF}}$. A comparable behavior is evident across all $\varepsilon_n\{2\}$ values derived from the NLEFT calculations. While a similar trend is observed for both ε_2 and ε_4 in the VMC results, notable deviations are present for ε_3 at all centralities. However, the differences between the NLEFT and VMC results can be quantitatively explained using ARM calculations for ε_3 and ε_4 . To illustrate this, we present the differences between OC configurations and the nucleon configurations obtained through ARM in the bottom plots. To assess the sensitivity of ARM to collision energies, we compare results from collisions at 200 GeV (top panels) and 5.36 TeV (bottom panels). The results for $\varepsilon_3\{2\}$ from NLEFT indicate the large deviations from ARM occur in central collisions, where ARM captures approximately 97% of the NLEFT information

at 200 GeV and 96% at 5.36 TeV. In contrast, the differences for VMC fall within the range of 2-4%, with large deviations observed at higher centralities. Overall, the results for ε_3 demonstrate robustness across different collision energy scales. The behavior of $\varepsilon_4\{2\}$ exhibits some differences. Both NLEFT and VMC results show sensitivity to the center-of-mass energies. Notably, maximum deviations for NLEFT are observed in the 10-20% centrality range, while VMC shows these deviations at 0-5% centrality. A larger discrepancy between VMC and ARM is noted for $\varepsilon_4\{2\}$ compared to $\varepsilon_3\{2\}$. Additionally, the ratio OC to ARM for ε_2 converges towards 1 as centrality increases, suggesting that similar ratios are also approximately achieved for ε_3 and ε_4 across all centralities.

In Ref.[13], it was noted for the first time that the relevant differences between the configurations in observables are angular rather than solely dependent on radial information. The authors fitted 3pF density to the nucleon configurations obtained from the models. A key aspect of our approach, is that we start with the same radial density, specifically the 3pF distribution, to reconstruct the NN correlations of *ab-initio* models. Consequently, any differences between configurations are attributed to their angular components. As demonstrated in our results,

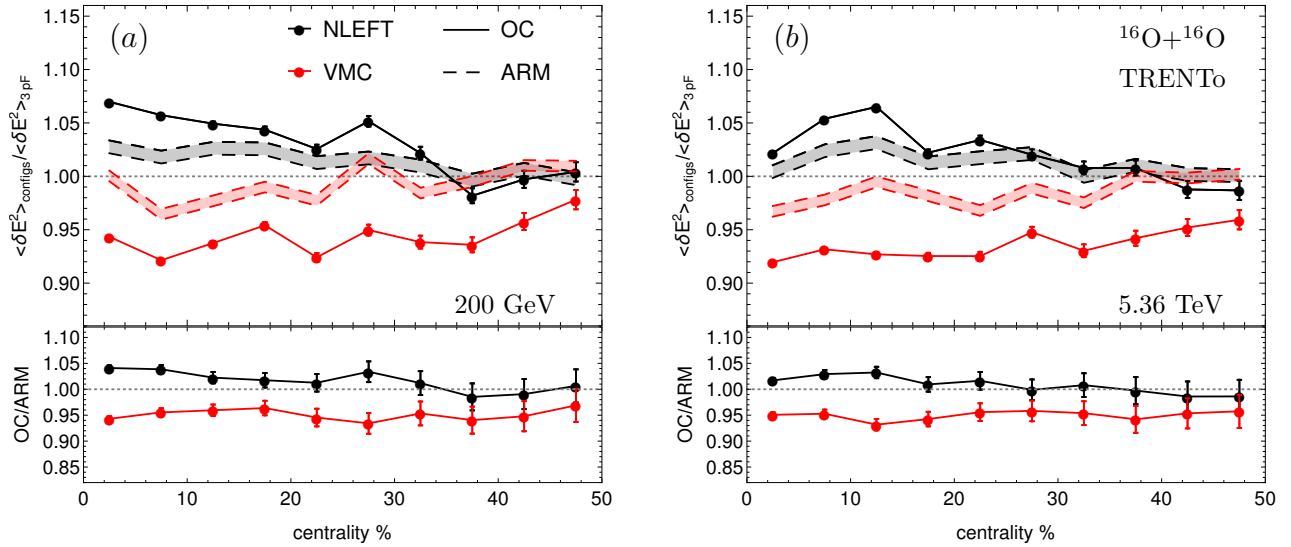


FIG. 4. The variance of the total system energy density created in $^{16}\text{O} + ^{16}\text{O}$ collisions is shown. To better assess the performance of the ARM method, the ratios of OC (solid lines) and ARM (dashed lines) configurations with respect to the 3pF model are depicted. The results from NLEFT and VMC are presented by black and red lines, respectively. The variance for different collision energies is illustrated in panels (a) and (b) for 200 GeV and 5.36 TeV, respectively. The bottom plots present the differences between the OC and ARM configurations.

the ARM confirms the significance of angular effects on the $\varepsilon_n\{2\}$. This observation is not limited to these correlators; similar conclusions can be drawn from other correlators, such as $\text{var}(E)$, $\text{cov}(\varepsilon_n^2, \delta E)$, as we will see in the following. Furthermore, the differences observed between OC and ARM configurations suggest that the acceptance-rejection method does not fully capture all angular information.

The nuclear structure information encoded in the collision area can also be reconstructed by averaging the transverse momenta of hadrons [7, 41]:

$$[p_T] = (1/N_{ch}) \sum_{i=1}^{N_{ch}} p_{T,i}.$$

According to the hydrodynamic paradigm, $[p_T]$ is not only influenced by the transverse size of fireball but can also provide insight into the amount of energy concentrated in the collision area [42]. This implies that a detail examination of NN correlation effects can yield additional information when we analyze the fluctuations in total energy density [43]:

$$E = \int_{x,y} \epsilon(x, y),$$

where $\epsilon(\mathbf{x}, \mathbf{y})$ presents the transverse energy density distribution in a single event. The fluctuations of E can be derived from the variance of energy [35]:

$$\langle \delta p_T^2 \rangle \propto \langle \delta E^2 \rangle = \frac{\langle E^2 \rangle_{ev} - \langle E \rangle_{ev}^2}{\langle E \rangle_{ev}^2}, \quad (11)$$

where $\langle \dots \rangle_{ev}$ denotes the average over all events. The results for $\langle \delta E^2 \rangle$ are presented in Fig.4. The red lines indicate the variance from VMC, while the results from NLEFT are shown with black lines. The top plots display the ratio $\langle \delta E^2 \rangle_{\text{configs}} / \langle \delta E^2 \rangle_{\text{3pF}}$. Solid and dashed lines represent calculations related to OC and ARM, respectively.

Our findings suggest that different types of correlations have varying effects on $\text{var}(E)$ observed between NLEFT and VMC. Notably, ARM quantitatively captures the trends of OC for both 200 GeV and 5.36 TeV, despite some deviations. This discrepancy is more pronounced for VMC, as illustrated in the bottom plots. Fig.4 indicates that the maximum deviation from OC occurs in central collisions. The results for OC and ARM are more consistent at 5.36 TeV, particularly for NLEFT. This may be attributed to the small differences in $\rho(r)$ between NLEFT and 3pF, which lead to improved angular reconstruction compared to VMC. Additionally, this convergence of NLEFT towards ARM occurs more rapidly than for VMC at higher centralities. Ultimately, the variance results reaffirm that the various distance-distance correlation effects can be effectively restored using ARM.

Three-particle correlators: The collective expansion of the dense matter produced in the interaction region is most commonly assessed by examining the azimuthal asymmetry of emitted hadrons and transverse momentum spectra [44], as illustrated in Figs.3 and 4. Correlations between the average transverse flow and the coefficients of azimuthally asymmetric flow [45, 46] may reveal significant insights regarding the relationship in the initial state between energy density and the eccentricities

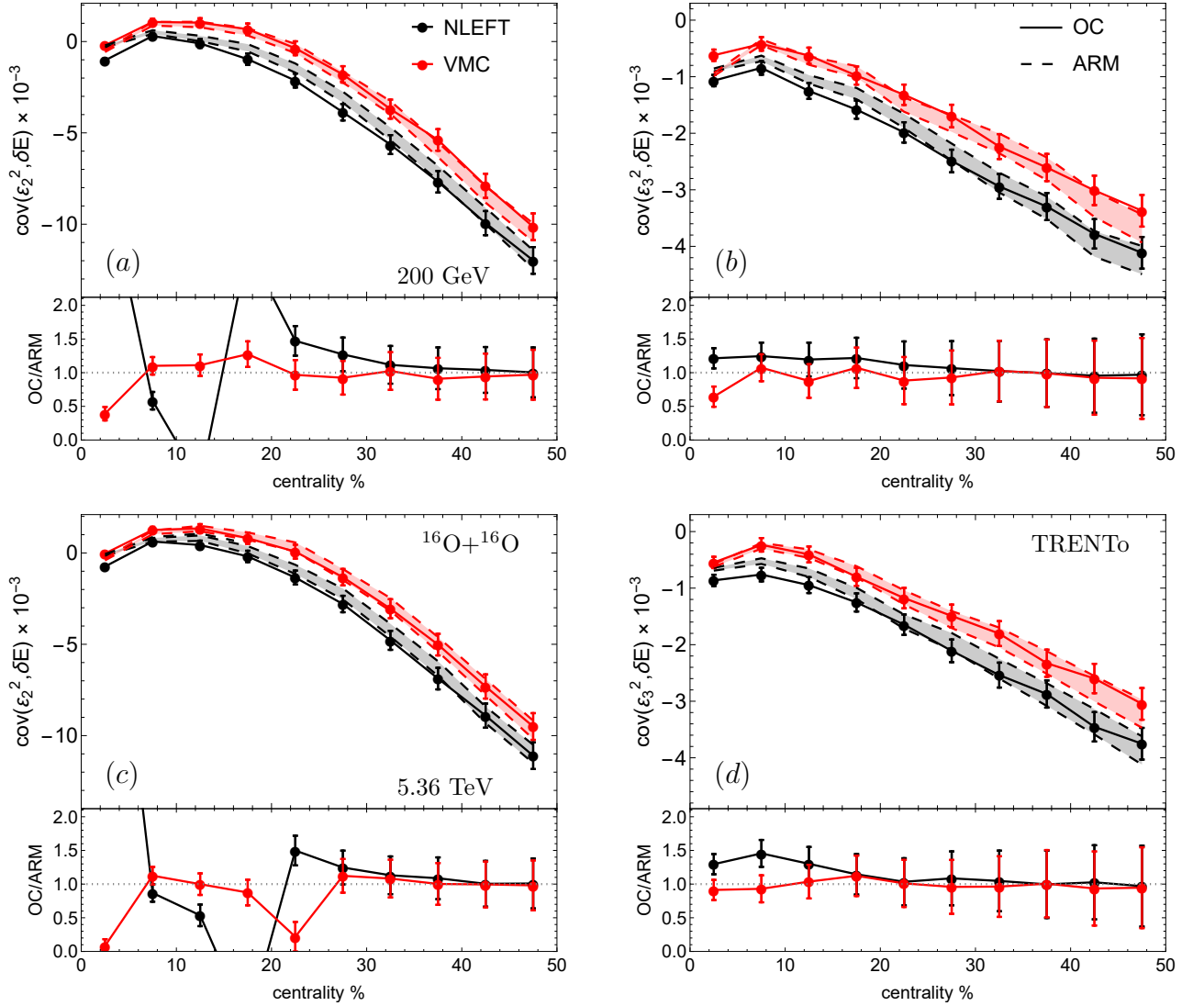


FIG. 5. The results of three-particle correlations are displayed for OC (solid lines) and ARM (dashed lines). The covariances, $\text{cov}(\varepsilon_2^2, \delta E)$ and $\text{cov}(\varepsilon_3^2, \delta E)$, are presented in the left and right panels, respectively. The bottom plots show the differences between the OC and ARM calculations. Additionally, we present the results obtained from O+O collisions at 200 GeV and 5.36 TeV in the top and bottom panels, respectively.

[42]:

$$\text{cov}(v_n^2, \delta p_T) \propto \text{cov}(\varepsilon_n^2, \delta E) = \frac{\langle \varepsilon_n^2 E \rangle_{ev}}{\langle E \rangle_{ev}} - \varepsilon_n^2 \{2\}. \quad (12)$$

Furthermore, the flow-transverse momentum correlation serves as a crucial factor in determining nuclear structures [40]. We employ this correlation to evaluate the performance of the acceptance-rejection method in comparison with OC results. The findings are presented in Fig.5, where the correlations $\text{cov}(\varepsilon_2^2, \delta E)$ and $\text{cov}(\varepsilon_3^2, \delta E)$ are shown in left and right panels, respectively. Additionally, the sensitivity to collision energies is examined in the top plots for 200 GeV and in the bottom plots for 5.36 TeV. The results of $\varepsilon_n - E$ correlations are depicted in this figure for NLEFT (black lines) and VMC

(red lines). Notably, the correlator helps to explain the differences between the structures obtained by *ab-initio* models, even at higher centralities.

As illustrated in Fig.5, in central (0-5%) collisions, the trends observed in VMC results are more accurately represented by $\text{cov}(\varepsilon_2^2, \delta E)$ at both 200 GeV and 5.36 TeV, as well as by $\text{cov}(\varepsilon_3^2, \delta E)$ at 5.36 TeV calculated using ARM configurations. Conversely, $\text{cov}(\varepsilon_3^2, \delta E)$ demonstrates good consistency with NLEFT at 200 GeV. At higher centralities, ARM calculations show agreement with OC results, as depicted in the bottom plots, which also capture the differences within OC results. It is important to note that the significant variations observed in the bottom plots arise from some points being close to zero.

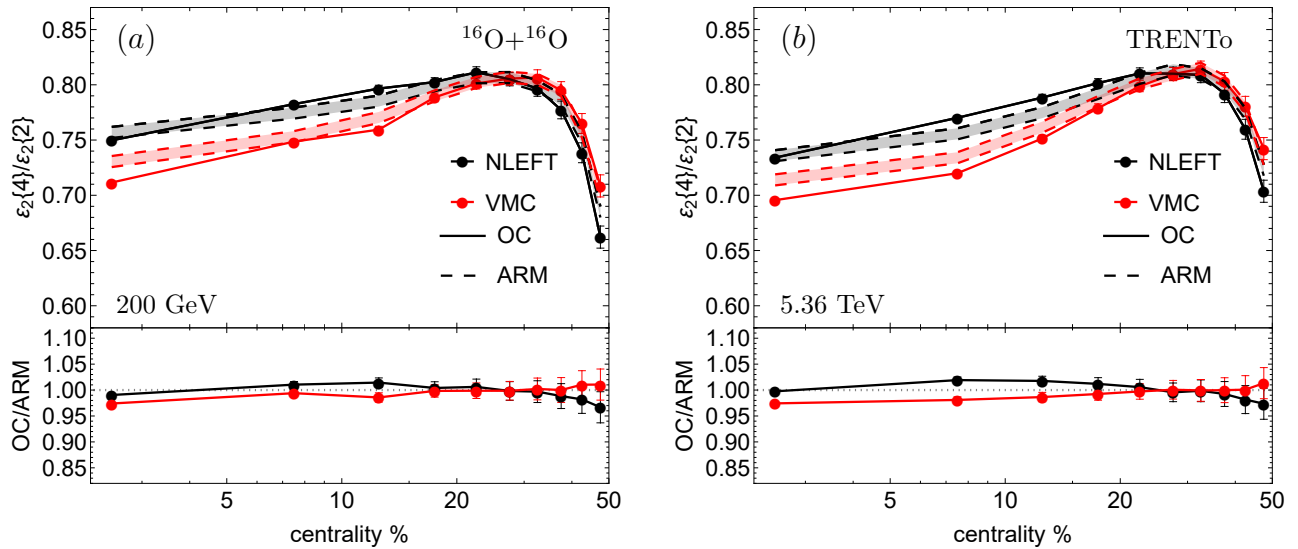


FIG. 6. Relative eccentricity fluctuation, $\varepsilon_2\{4\}/\varepsilon_2\{2\}$, is plotted as a function of centrality percentile in $^{16}\text{O} + ^{16}\text{O}$ collisions at 200 GeV (left panel) and 5.36 TeV (right panel). Solid lines represent the original configurations, while ARM calculations are shown with dashed lines.

Four-particle correlators: Since ^{16}O is doubly magic and nearly spherical in a mean-field description [47], many-body correlations can deform it into an irregular tetrahedral structure with α -like clusters forming its edges [12, 17]. The influence of these clusters on the initial geometry fluctuations differs significantly from the predictions made by NLEFT and VMC [8]. The initial geometric fluctuations can be quantified using the ratio $\varepsilon_2\{4\}/\varepsilon_2\{2\}$, defined as follows:

$$\begin{aligned} \varepsilon_2\{2\} &= \langle \varepsilon_2^2 \rangle^{1/2}, \\ \varepsilon_2\{4\} &= (2\langle \varepsilon_2^2 \rangle^2 - \langle \varepsilon_2^4 \rangle)^{1/4}. \end{aligned} \quad (13)$$

This relative fluctuation in eccentricity is crucial for understanding the hydrodynamic response, which presents a linear relationship between elliptic flow v_2 and the participant-plane eccentricity within a given centrality class, expressed as $v_2 \propto \varepsilon_2$. We can approximate this relation as $v_2\{4\}/v_2\{2\} \approx \varepsilon_2\{4\}/\varepsilon_2\{2\}$, allowing for higher precision measurements through initial-state calculations.

In Fig.6, we present the results for $\varepsilon_2\{4\}/\varepsilon_2\{2\}$ derived from nucleon configurations produced by the NLEFT (black lines) and VMC (red lines) approaches. Data were generated for O+O collisions at both 200 GeV (left panel) and 5.36 TeV (right panel). Additionally, we include results from ARM calculations, represented by dashed lines in this figure. The trends observed in ARM closely follow those of OC, and the differences between various models are explained through ARM calculations. Notably, better consistency is evident in the results for collisions at 200 GeV. While the ratio appears sensitive to collision energy, the discrepancy between OC and ARM is less than 5% at 5.36 TeV. The maximum deviation from OC

is observed for VMC in the 0-5% centrality range; however, both OC and ARM calculated ratios demonstrate good agreement overall.

IV. CONCLUSION

Given that nucleons are not entirely independent particles within the nucleus, the interactions between nucleons become essential for understanding nuclear structures. In this paper, we investigated the nucleon-nucleon correlations encoded in the nucleon configurations of ^{16}O , generated through NLEFT and VMC approaches, employing an acceptance-rejection method (ARM). In our approach, we utilized a three-parameter Fermi density to define the radial distribution of nucleons and randomly generated angular coordinates for each nucleon. To replicate the configurations produced by the models, we accepted samples that met the acceptance condition based on a uniform distribution. Our findings demonstrate that ARM can effectively and quantitatively decode nucleon-nucleon correlations in *ab-initio* models. To showcase the capabilities of ARM, we analyzed various correlation functions, including two-particle correlations ($\text{var}(E)$ and $\varepsilon_n\{2\}$), three-particle correlations ($\text{cov}(\varepsilon_n^2, \delta E)$), and four-particle correlations ($\varepsilon_2\{4\}/\varepsilon_2\{2\}$), as detailed in Section III. The results indicated that the three- and four-particle correlators derived from the ARM calculations exhibit a higher degree of consistency with the NLEFT and VMC models. This alignment suggests that the ARM approach effectively captures the underlying dynamics of the system, reinforcing its validity in analyzing particle correlations in $^{16}\text{O} + ^{16}\text{O}$ collisions. Additionally, we explored the transverse size of the fireball,

revealing that ARM effectively captures system size information in the overlap region.

From our calculations, two significant results emerge. The first pertains to short-distance correlations, which are evident in the differences observed in $C(\Delta r)$ for NLEFT and VMC at distances approximately less than 1 fm. Our analysis demonstrates that the ARM effectively captures these short-range correlations, as illustrated by the distance-distance $C(\Delta r)$ distribution. The results indicate that variations in $C(\Delta r)$ significantly influence the correlators, suggesting that the structural differences between light nuclei can be attributed to the correlations present within each α -cluster. However, this insight alone does not provide a complete picture; the radial distributions also play a crucial role in elucidating the underlying nuclear structure information. The second key finding relates to the differences in angular coordinates. Our results reveal that the distinctions between NLEFT and VMC are not solely a consequence of the radial distributions; rather, they also stem from angular effects. This conclusion is supported by our analysis, which assumes a fixed distribution and highlights the discrepancies between the ARM results for NLEFT and VMC. Together, these findings underscore the importance of both radial

and angular correlations in understanding the complex structure of light nuclei.

Although the acceptance-rejection method can accurately reproduce the distance-distance correlations, the correlator results indicate that ARM quantitatively decodes structural information. This finding suggests a need to explore the constraints arising from 3- or 4-body densities, an endeavor we intend to pursue in future work due to the inherent complexity of these multi-particle correlations. Such investigations are essential for extracting comprehensive insights from *ab-initio* models. Furthermore, it would be beneficial to extend this study to other light nuclei, such as ^8Be , ^{12}C , and ^{20}Ne , in order to assess the sensitivity of the presented method to varying sizes and structures. This broader analysis could enhance our understanding of the nuclear interactions at play and further validate the robustness of the ARM approach.

ACKNOWLEDGEMENTS

H.M is supported in part by the National Natural Science Foundation of China under Grant No. 12247107. B.N.Lu is also supported by the National Security Academic Fund (Grant No.U2330401).

[1] M. Freer, H. Horiuchi, Y. Kanada-En'yo, D. Lee, and U.-G. Meißner, *Rev. Mod. Phys.* **90**, 035004 (2018), arXiv:1705.06192 [nucl-th].

[2] R. Cruz-Torres, D. Lonardoni, R. Weiss, N. Barnea, D. W. Higinbotham, E. Piasetzky, A. Schmidt, L. B. Weinstein, R. B. Wiringa, and O. Hen, *Nature Phys.* **17**, 306 (2021), arXiv:1907.03658 [nucl-th].

[3] A. Schmidt *et al.* (CLAS), *Nature* **578**, 540 (2020), arXiv:2004.11221 [nucl-ex].

[4] Q.-R. Lin, Y.-J. Huang, L.-G. Pang, X.-F. Luo, and X.-N. Wang, (2025), arXiv:2503.01128 [hep-ph].

[5] M. Piarulli and I. Tews, *Front. in Phys.* **7**, 245 (2020), arXiv:2002.00032 [nucl-th].

[6] M. Piarulli, J. Bub, and I. Tews, “Local Two- and Three-Nucleon Interactions Within Chiral Effective Field Theory,” in *Handbook of Nuclear Physics*, edited by I. Tanihata, H. Toki, and T. Kajino (2022) pp. 1–33.

[7] G. Giacalone *et al.*, (2025), arXiv:2507.01454 [nucl-ex].

[8] S. Huang (2023) arXiv:2312.12167 [nucl-ex].

[9] Z. Citron *et al.*, CERN Yellow Rep. Monogr. **7**, 1159 (2019), arXiv:1812.06772 [hep-ph].

[10] J. Brewer, A. Mazeliauskas, and W. van der Schee, in *Opportunities of OO and pO collisions at the LHC* (2021) arXiv:2103.01939 [hep-ph].

[11] H. Mehrabpour and A. Saha, (2025), arXiv:2501.14243 [nucl-th].

[12] G. Giacalone *et al.*, (2024), arXiv:2402.05995 [nucl-th].

[13] C. Zhang, J. Chen, G. Giacalone, S. Huang, J. Jia, and Y.-G. Ma, (2024), arXiv:2404.08385 [nucl-th].

[14] M. Alvioli, H. J. Drescher, and M. Strikman, *Phys. Lett. B* **680**, 225 (2009), arXiv:0905.2670 [nucl-th].

[15] Y.-J. Huang, Z. Meng, L.-G. Pang, and X.-N. Wang, (2025), arXiv:2504.00790 [nucl-th].

[16] W. Broniowski and E. Ruiz Arriola, *Phys. Rev. Lett.* **112**, 112501 (2014), arXiv:1312.0289 [nucl-th].

[17] H. Mehrabpour, (2025), arXiv:2506.12673 [nucl-th].

[18] J.-P. Blaizot and G. Giacalone, (2025), arXiv:2504.15421 [nucl-th].

[19] J.-Y. Hu, H.-j. Xu, X. Wang, and S. Pu, (2025), arXiv:2507.01493 [nucl-th].

[20] B.-N. Lu, N. Li, S. Elhatisari, D. Lee, E. Epelbaum, and U.-G. Meißner, *Phys. Lett. B* **797**, 134863 (2019), arXiv:1812.10928 [nucl-th].

[21] S. Elhatisari, E. Epelbaum, H. Krebs, T. A. Lähde, D. Lee, N. Li, B.-n. Lu, U.-G. Meißner, and G. Rupak, *Phys. Rev. Lett.* **119**, 222505 (2017), arXiv:1702.05177 [nucl-th].

[22] D. Lonardoni, A. Lovato, S. C. Pieper, and R. B. Wiringa, *Phys. Rev. C* **96**, 024326 (2017), arXiv:1705.04337 [nucl-th].

[23] M. Alvioli, C. Ciofi degli Atti, and H. Morita, *Phys. Rev. C* **72**, 054310 (2005), arXiv:nucl-th/0506054.

[24] V. R. Pandharipande and R. B. Wiringa, *Rev. Mod. Phys.* **51**, 821 (1979).

[25] M. Rybczyński and W. Broniowski, *Phys. Rev. C* **100**, 064912 (2019), arXiv:1910.09489 [hep-ph].

[26] S. C. Pieper, R. B. Wiringa, and V. R. Pandharipande, *Phys. Rev. C* **46**, 1741 (1992).

[27] G. Baym, B. Blattel, L. L. Frankfurt, H. Heiselberg, and M. Strikman, *Phys. Rev. C* **52**, 1604 (1995), arXiv:nucl-th/9502038.

[28] H. Heiselberg, *Phys. Rept.* **351**, 161 (2001), arXiv:nucl-th/0003046.

- [29] R. Christensen, A. Branscum, and T. E Hanson, “Bayesian Ideas and Data Analysis: An Introduction for Scientists and Statisticians,” in *Chapman and Hall/CRC Texts in Statistical Science* (2010) 1st ed.
- [30] I. Angeli and K. Marinova, *Atomic Data and Nuclear Data Tables* **99**, 69 (2013).
- [31] J. S. Moreland, J. E. Bernhard, and S. A. Bass, *Phys. Rev. C* **92**, 011901 (2015), arXiv:1412.4708 [nucl-th].
- [32] C. Loizides, (2025), arXiv:2507.05853 [nucl-th].
- [33] B. Schenke, P. Tribedy, and R. Venugopalan, *Phys. Rev. C* **86**, 034908 (2012), arXiv:1206.6805 [hep-ph].
- [34] B. Schenke and S. Schlichting, *Phys. Rev. C* **94**, 044907 (2016), arXiv:1605.07158 [hep-ph].
- [35] G. Giacalone, F. G. Gardim, J. Noronha-Hostler, and J.-Y. Ollitrault, *Phys. Rev. C* **103**, 024909 (2021), arXiv:2004.01765 [nucl-th].
- [36] F. G. Gardim, G. Giacalone, M. Luzum, and J.-Y. Ollitrault, *Nucl. Phys. A* **1005**, 121999 (2021), arXiv:2002.07008 [nucl-th].
- [37] R. Samanta, S. Bhatta, J. Jia, M. Luzum, and J.-Y. Ollitrault, *Phys. Rev. C* **109**, L051902 (2024), arXiv:2303.15323 [nucl-th].
- [38] P. Bozek and W. Broniowski, *Phys. Rev. C* **85**, 044910 (2012), arXiv:1203.1810 [nucl-th].
- [39] P. Božek and W. Broniowski, *Phys. Rev. C* **96**, 014904 (2017), arXiv:1701.09105 [nucl-th].
- [40] J. Jia, *Phys. Rev. C* **105**, 044905 (2022), arXiv:2109.00604 [nucl-th].
- [41] J. Jia *et al.*, *Nucl. Sci. Tech.* **35**, 220 (2024), arXiv:2209.11042 [nucl-ex].
- [42] G. Giacalone, *Eur. Phys. J. A* **59**, 297 (2023), arXiv:2305.19843 [nucl-th].
- [43] J.-P. Blaizot, W. Broniowski, and J.-Y. Ollitrault, *Phys. Lett. B* **738**, 166 (2014), arXiv:1405.3572 [nucl-th].
- [44] C. Gale, S. Jeon, and B. Schenke, *Int. J. Mod. Phys. A* **28**, 1340011 (2013), arXiv:1301.5893 [nucl-th].
- [45] P. Bozek, *Phys. Rev. C* **93**, 044908 (2016), arXiv:1601.04513 [nucl-th].
- [46] P. Bozek and H. Mehrabpour, *Phys. Rev. C* **101**, 064902 (2020), arXiv:2002.08832 [nucl-th].
- [47] J. P. Delaroche, M. Girod, J. Libert, H. Goutte, S. Hilaire, S. Peru, N. Pillet, and G. F. Bertsch, *Phys. Rev. C* **81**, 014303 (2010), arXiv:0910.2940 [nucl-th].